



# Surface effects on shape and topology optimization of nanostructures

S. S. Nanthakumar<sup>1</sup> · Navid Valizadeh<sup>1</sup> · Harold S. Park<sup>2</sup> · Timon Rabczuk<sup>1,3</sup>

Received: 20 January 2015 / Accepted: 25 April 2015 / Published online: 14 May 2015  
© Springer-Verlag Berlin Heidelberg 2015

**Abstract** We present a computational method for the optimization of nanostructures, where our specific interest is in capturing and elucidating surface stress and surface elastic effects on the optimal nanodesign. XFEM is used to solve the nanomechanical boundary value problem, which involves a discontinuity in the strain field and the presence of surface effects along the interface. The boundary of the nanostructure is implicitly represented by a level set function, which is considered as the design variable in the optimization process. Two objective functions, minimizing the total potential energy of a nanostructure subjected to a material volume constraint and minimizing the least square error compared to a target displacement, are chosen for the numerical examples. We present results of optimal topologies of a nanobeam subject to cantilever and fixed boundary conditions. The numerical examples demonstrate the importance of size and aspect ratio in determining how surface effects impact the optimized topology of nanobeams.

---

✉ Harold S. Park  
parkhs@bu.edu

✉ Timon Rabczuk  
timon.rabczuk@uni-weimar.de

S. S. Nanthakumar  
nanthakumar.srividiputtur.subbiah@uni-weimar.de

Navid Valizadeh  
navid.valizadeh@uni-weimar.de

<sup>1</sup> Institute of Structural Mechanics, Bauhaus-Universität Weimar, Marienstraße 15, 99423 Weimar, Germany

<sup>2</sup> Department of Mechanical Engineering, Boston University, 730 Commonwealth Avenue, ENA 212, Boston, MA 02215, USA

<sup>3</sup> School of Civil, Environmental and Architectural Engineering, Korea University, Seoul, Republic of Korea

**Keywords** Nanomaterials · Surface effects · Shape optimization · Extended finite element method (XFEM) · Level set method

## 1 Introduction

Due to their unique physical properties [1, 2], nanostructures have recently attracted significant attention from the scientific community. In addition to their electronic, thermal and optical properties, nanostructures can exhibit mechanical behavior and properties that are superior to those of the corresponding bulk material. The underlying physical mechanism for the changes in the mechanical, and other physical properties with decreasing structure size, is the increasing significance of surface effects, which is due to increasing surface area to volume ratio [3].

The physical origin of the surface effects is that atoms at the surfaces of a material have fewer bonding neighbors than atoms that lie within the material bulk [4]. This so-called undercoordination of the surface atoms causes them to exhibit different elastic properties than atoms in the bulk, which can lead to either stiffening or softening of the nanostructure, as described by Zhou and Huang [5] and recently reviewed by Park et al [6]. Surface effects also have a first order effect on the deformation mechanisms and plasticity in nanostructures, as illustrated in various works [7–9] and recently summarized by Weinberger and Cai [10]. Therefore, it is critical to consider surface effects when discussing the mechanical behavior and properties of nanomaterials, particularly when any characteristic dimension of the nanostructure is smaller than about 100 nm [6].

These unique mechanical properties have motivated researchers to develop computational approaches that capture

these surface effects based on either linear or nonlinear continuum theories. For example, many computational approaches [11–14] are based on the well-known Gurin–Murdoch linear surface elasticity theory [15], which considers the surface to be an entity of zero thickness that has its own elastic properties that are distinct from the bulk. Other approaches have considered a bulk plus surface ansatz of various forms incorporating finite deformation kinematics. The approaches not bound on the Gurin–Murdoch framework include the work by Steinmann and co-workers [16,17], and the surface Cauchy–Born approach of Park and co-workers [18–20]. The interested reader is also referred to the recent review of Javili et al [21].

However, most theoretical and computational studies have focused on determining how surface effects impact specific mechanical properties, i.e. the Young’s modulus [6], plastic deformation mechanisms [7,10], resonant frequencies [22,23], bending response [24,25], and more generally the mechanical response of nanostructures such as nanowires or nanobeams. What has not been done to-date is to investigate how surface effects impact the topology of nanostructures within the concept of optimally performing structures. This topic has a significant history and literature for bulk materials [26–28], but has not been studied for surface-dominated nanostructures.

The objective of this work is therefore to present a numerical method that can be used to study the optimization of nanostructures, while accounting for the critical physics of interest, that of nanoscale surface effects. The formulation is general, and can be applied to different materials such as FCC metals or silicon so long as the relevant surface elastic constants are known. This is done through a coupling of the extended finite element method (XFEM) [29] and the level set method [27]. By using XFEM to solve the nanomechanical boundary value problem including surface effects based on Gurin–Murdoch surface elasticity theory [11,14,15], we are able to maintain a fixed background FE mesh while only the structural topology varies. The level set method (LSM) in which the front velocity is derived from a shape sensitivity analysis by solving an adjoint problem is based on the ideas proposed by Allaire et al.[27].

The outline of the paper is as follows. In Sect. 2, based on Gurin–Murdoch surface elasticity theory [15], the continuum model for an elastic solid considering surface effects is presented. Section 3 illustrates the LSM for structural optimization. In Sect. 4, the objective functions and the material derivative for shape sensitivity analysis are presented. A brief overview on the XFEM formulation is given in Sect. 5 followed by numerical examples in Sect. 6, and finally concluding remarks.

## 2 Continuum model

We consider an elastic solid  $\Omega$  with a material surface  $\partial\Omega$ . According to continuum theory of elastic material surfaces [15], the equilibrium equations for a nanostructure can be written as:

$$\nabla \cdot \sigma + b = 0 \quad \text{in } \Omega \quad (1)$$

$$\nabla_s \cdot \sigma_s + [\sigma \cdot \mathbf{n}] = 0 \quad \text{on } \Gamma \quad (2)$$

where the first equation refers to bulk equilibrium and the second equation refers to the generalized Young-Laplace Eq. [15] resulting from mechanical equilibrium on the surface. In the above equations,  $\sigma$  represents bulk Cauchy stress tensor,  $b$  represents the body force vector,  $\sigma_s$  denotes the surface stress tensor,  $\mathbf{n}$  is the outward unit normal vector to  $\Gamma$ , and  $\nabla_s \cdot \sigma_s = \nabla \sigma_s : \mathbf{P}$ . Here  $\mathbf{P}$  is the tangential projection tensor to  $\Gamma$  at  $\mathbf{x} \in \Gamma$  which is defined as  $\mathbf{P}(\mathbf{x}) = \mathbf{I} - \mathbf{n}(\mathbf{x}) \otimes \mathbf{n}(\mathbf{x})$ ,  $\mathbf{I}$  is the second order unit tensor.  $\Gamma$  is the boundary of the domain  $\Omega$ . Furthermore, the boundary conditions are given by

$$\begin{aligned} \sigma \cdot \mathbf{n} &= \bar{\mathbf{t}} && \text{on } \Gamma_N \\ \mathbf{u} &= \bar{\mathbf{u}} && \text{on } \Gamma_D \end{aligned} \quad (3)$$

where  $\bar{\mathbf{t}}$  and  $\bar{\mathbf{u}}$  are the prescribed traction and displacement, respectively, and  $\Gamma_N$  and  $\Gamma_D$  are the Neumann and Dirichlet boundaries. The bulk strain tensor  $\epsilon$  and surface strain tensor  $\epsilon_s$  are written as

$$\epsilon = \frac{1}{2} (\nabla \mathbf{u} + (\nabla \mathbf{u})^T) \quad (4)$$

$$\epsilon_s = \mathbf{P} \cdot \epsilon \cdot \mathbf{P} \quad (5)$$

where  $\mathbf{u}$  is the displacement vector. Assuming a linear elastic bulk material and an isotropic linear elastic surface, the constitutive equations for the bulk and surface can be written as

$$\sigma = \mathbb{C}^{bulk} : \epsilon \quad (6)$$

$$\sigma_s = \frac{\partial \gamma}{\partial \epsilon_s} \quad (7)$$

where  $\gamma$  is the surface energy density given by

$$\gamma = \gamma_0 + \tau_s : \epsilon_s + \frac{1}{2} \epsilon_s : \mathbb{C}^s : \epsilon_s \quad (8)$$

where  $\gamma_0$  is the surface free energy density that exists even when  $\epsilon_s = 0$ , and  $\tau_s = \tau_s \mathbf{P}$  is the surface residual stress tensor. By substituting Eq. 8 into Eq. 7,  $\sigma_s$  can be obtained by

$$\boldsymbol{\sigma}_s = \boldsymbol{\tau}_s + \mathbb{C}^s : \boldsymbol{\epsilon}_s \quad (9)$$

In the above equations,  $\mathbb{C}^{bulk}$  and  $\mathbb{C}^s$  are the fourth-order elastic stiffness tensors associated with the bulk and surface, respectively, and are defined as

$$\mathbb{C}_{ijkl}^{bulk} = \lambda \delta_{ij} \delta_{kl} + \mu (\delta_{ik} \delta_{jl} + \delta_{il} \delta_{jk}) \quad (10)$$

$$\mathbb{C}_{ijkl}^s = \lambda_s P_{ij} P_{kl} + \mu_s (P_{ik} P_{jl} + P_{il} P_{jk}) \quad (11)$$

where  $\lambda$  and  $\mu$ , and  $\lambda_s$  and  $\mu_s$  are the Lamé constants of the bulk and surface, respectively.

It should be noted that the surface is considered as a special case of a coherent imperfect interface between two materials when one of them exists in a vacuum phase [12]. It is assumed that the surface adheres to the bulk and therefore we have:

$$[\![\mathbf{u}]\!] = 0 \quad (\text{i.e.}) \quad (\mathbf{u})^+ - (\mathbf{u})^- = 0 \quad \text{on } \Gamma \quad (12)$$

where  $[\![\cdot]\!]$  denotes the jump across the interface.

Having defined the constitutive and field equations, we derive the weak form of the boundary value problem based on the principle of stationary potential energy. The total potential energy  $\Pi$  of the system is given by

$$\Pi = \Pi_{bulk} + \Pi_s - \Pi_{ext} \quad (13)$$

where  $\Pi_{bulk}$ ,  $\Pi_s$ , and  $\Pi_{ext}$  represent the bulk elastic strain energy, surface elastic energy and the work of external forces, respectively, which are given by

$$\Pi_{bulk} = \frac{1}{2} \int_{\Omega} \boldsymbol{\epsilon} : \mathbb{C}^{bulk} : \boldsymbol{\epsilon} d\Omega \quad (14)$$

$$\Pi_s = \int_{\Gamma} \gamma d\Gamma \quad (15)$$

$$\Pi_{ext} = \int_{\Gamma_N} \mathbf{u} \cdot \bar{\mathbf{t}} d\Gamma + \int_{\Omega} \mathbf{u} \cdot \mathbf{b} d\Omega \quad (16)$$

The stationary condition of Eq. 13 is given by

$$D_{\delta \mathbf{u}} \Pi = 0 \quad (17)$$

where  $D_{\mathbf{m}} \Upsilon$  is the directional derivative (or Gâteaux derivative) of the functional  $\Upsilon$  in the direction  $\mathbf{m}$ . Applying the stationary condition, the weak form of the equilibrium equations can be obtained by finding  $\mathbf{u} \in \{\mathbf{u} = \bar{\mathbf{u}} \text{ on } \Gamma_D, \mathbf{u} \in H^1(\Omega)\}$  such that

$$\begin{aligned} & \int_{\Omega} \boldsymbol{\epsilon}(\mathbf{u}) : \mathbb{C}^{bulk} : \boldsymbol{\epsilon}(\delta \mathbf{u}) d\Omega + \int_{\Gamma} \boldsymbol{\epsilon}_s(\mathbf{u}) : \mathbb{C}^s : \boldsymbol{\epsilon}_s(\delta \mathbf{u}) d\Gamma \\ &= - \int_{\Gamma} \boldsymbol{\tau}_s : \boldsymbol{\epsilon}_s(\delta \mathbf{u}) d\Gamma + \int_{\Gamma_N} \delta \mathbf{u} \cdot \bar{\mathbf{t}} d\Gamma + \int_{\Omega} \delta \mathbf{u} \cdot \mathbf{b} d\Omega \end{aligned} \quad (18)$$

for all  $\delta \mathbf{u} \in \{\delta \mathbf{u} = 0 \text{ on } \Gamma_D, \delta \mathbf{u} \in H^1(\Omega)\}$ . This weak form can be written in a simplified form as

$$a(\mathbf{u}, \delta \mathbf{u}) + a_s(\mathbf{u}, \delta \mathbf{u}) = -l_s(\delta \mathbf{u}) + l(\delta \mathbf{u}) \quad (19)$$

where the bilinear functionals  $a(\mathbf{u}, \delta \mathbf{u})$  and  $a_s(\mathbf{u}, \delta \mathbf{u})$ , and linear functionals  $l(\delta \mathbf{u})$  and  $l_s(\delta \mathbf{u})$  are defined as

$$\begin{aligned} a(\mathbf{u}, \delta \mathbf{u}) &= \int_{\Omega} \boldsymbol{\epsilon}(\mathbf{u}) : \mathbb{C}^{bulk} : \boldsymbol{\epsilon}(\delta \mathbf{u}) d\Omega = \int_{\Omega} \boldsymbol{\epsilon}(\mathbf{u}) : \mathbb{C}^s : \boldsymbol{\epsilon}_s(\delta \mathbf{u}) d\Omega \\ a_s(\mathbf{u}, \delta \mathbf{u}) &= \int_{\partial \Omega} c_s(\mathbf{u}, \delta \mathbf{u}) d\Gamma = \int_{\partial \Omega} \boldsymbol{\epsilon}_s(\mathbf{u}) : \mathbb{C}^s : \boldsymbol{\epsilon}_s(\delta \mathbf{u}) d\Gamma \\ l(\delta \mathbf{u}) &= \int_{\partial \Omega_N} \delta \mathbf{u} \cdot \bar{\mathbf{t}} d\Gamma + \int_{\Omega} \delta \mathbf{u} \cdot \mathbf{b} d\Omega \\ l_s(\delta \mathbf{u}) &= \int_{\partial \Omega} \boldsymbol{\tau}_s : \boldsymbol{\epsilon}_s(\delta \mathbf{u}) d\Gamma \end{aligned} \quad (20)$$

### 3 Level set method

The LSM, which was first introduced by Osher and Sethian [30] for tracking moving interfaces, has been extensively applied to many different research fields such as image processing, computer graphics, fluid mechanics, and crack propagation over the past three decades. The first research work on incorporating the LSM [30] in structural shape and topology optimization was performed by Sethian and Wiegmann [31]. They used the LSM to represent the design structure and to alter the design shape based on a Von Mises equivalent stress criterion. Later, Osher and Santosa [32], Allaire et al. [27], and Wang et al. [33] independently proposed a new class of structural optimization method based on a combination of the level set method with the shape sensitivity analysis framework. The main idea of this method is to model the process of structural optimization via a scalar level set function which dynamically changes in time. Therefore, the evolution of the design shape is governed by the Hamilton–Jacobi (H–J) partial differential equation (PDE) in which the front speed (or velocity vector) links the H–J equation with the shape sensitivity analysis. This method is usually called conventional LSM and is widely used in structural optimization [33, 34]. We note that there is no nucleation mechanism for new holes in this method. However the level-set method can easily handle topology changes, i.e. merging or vanishing of holes, and thus this algorithm can be used to perform topology optimization.

We assume  $\mathbf{D} \subset \mathbb{R}^d$  ( $d = 2$  or  $3$ ) as the whole structural shape and topology design domain including all admissible shapes  $\Omega$ , i.e.  $\Omega \subset \mathbf{D}$ . A level set function  $\Phi(\mathbf{x})$  which partitions the design domain  $\mathbf{D}$  into three parts, i.e. the solid, void and the boundary which are defined as

$$\begin{aligned} \text{Solid : } & \Phi(\mathbf{x}) < 0 \quad \forall \mathbf{x} \in \Omega \setminus \partial\Omega \\ \text{Boundary : } & \Phi(\mathbf{x}) = 0 \quad \forall \mathbf{x} \in \partial\Omega \cap \mathbf{D} \\ \text{Void : } & \Phi(\mathbf{x}) > 0 \quad \forall \mathbf{x} \in \mathbf{D} \setminus \Omega \end{aligned} \quad (21)$$

The basic idea of the LSM for structural optimization is to describe the structural design boundary  $\Gamma(\mathbf{x})$  implicitly by the zero level set of a higher dimensional level set function (see Fig. 1):

$$\Gamma(\mathbf{x}) = \left\{ \mathbf{x} \in \mathbb{R}^d \mid \Phi(\mathbf{x}) = 0 \right\} \quad (22)$$

To allow the design boundary for a dynamic evolution in the optimization process, we introduce  $t$  as a fictitious time. Thus the dynamic design boundary is defined as

$$\Gamma(t) = \left\{ \mathbf{x}(t) \in \mathbb{R}^d \mid \Phi(\mathbf{x}(t), t) = 0 \right\} \quad (23)$$

By differentiating  $\{\Phi(\mathbf{x}(t), t) = 0\}$  with respect to time<sup>1</sup>, we obtain the well-known Hamilton–Jacobi PDE

$$\frac{\partial \Phi(\mathbf{x}(t), t)}{\partial t} + \nabla \Phi(\mathbf{x}(t), t) \cdot \mathbf{V} = 0 \quad (24)$$

where  $\mathbf{V} = \frac{d\mathbf{x}}{dt}$  denotes the velocity vector of the design boundary. This equation can be further written considering the unit outward normal  $\mathbf{n} = \frac{\nabla \Phi}{|\nabla \Phi|}$  to the boundary and normal component of velocity vector  $V_n = \mathbf{V} \cdot \mathbf{n}$ ,

$$\frac{\partial \Phi}{\partial t} + V_n |\nabla \Phi| = 0 \quad (25)$$

By solving this Hamilton–Jacobi equation, the level set function and consequently the structural design boundary is updated during the optimization process. It should be noted that here  $V_n$  is a quantity that links the LSM to the shape design sensitivity analysis [33].

The Hamilton–Jacobi equations usually do not admit smooth solutions. Existence and uniqueness are achieved in the framework of viscosity solutions which provide a convenient definition of the generalized shape motion. The discrete solution of the H–J equation is obtained by an explicit first-order upwind scheme [27]. The level set function is regularized periodically by solving

$$\frac{\partial \Phi}{\partial t} + \text{sign}(\Phi_0) (\|\nabla \Phi\| - 1) = 0. \quad (26)$$

Solving this equation gives a signed distance function with respect to an initial isoline,  $\Phi_0$ . This ensures smooth interfaces and also that the signed distance from the interface can

be used as enrichment values for the nodes whose support is cut by the zero level sets, for the XFEM analysis performed in each iteration.

## 4 Material derivative approach and sensitivity analysis

In this work, we consider two objective functions. The first considers the total potential energy of the nanostructure under equilibrium and volume constraints. For this case, the topology optimization problem can be defined as

$$\text{Minimize } J_1(\Omega) = \int_{\Omega} \mathbf{u} \cdot \mathbf{b} d\Omega + \int_{\Gamma_N} \mathbf{u} \cdot \mathbf{t} d\Gamma \quad (27)$$

$$\text{Subject to } \int_{\Omega} d\Omega - \bar{V} = 0 \quad (28)$$

$$a(\mathbf{u}, \mathbf{v}, \Omega) + a_s(\mathbf{u}, \mathbf{v}, \Omega) = -l_s(\mathbf{v}, \Omega) + l(\mathbf{v}, \Omega) \quad (29)$$

The second is a least square error objective function compared to a target displacement, which can be written as

$$\text{Minimize } J_2(\Omega) = \left( \int_{\Gamma} |\mathbf{u} - \mathbf{u}_0|^2 d\Gamma \right)^{\frac{1}{2}} \quad (30)$$

$$\text{Subject to} \quad (31)$$

$$a(\mathbf{u}, \mathbf{v}, \Omega) + a_s(\mathbf{u}, \mathbf{v}, \Omega) = -l_s(\mathbf{v}, \Omega) + l(\mathbf{v}, \Omega) \quad (32)$$

Here we assume  $\mathbf{v} = \delta \mathbf{u}$  and  $\gamma_0 = 0$ . To perform shape optimization, it is essential to find the relationship between a variation in design variables and the resulting variations in cost functional [35] using a sensitivity analysis method. For this purpose, we use the material derivative concept from continuum mechanics.

### 4.1 Material derivative

Consider an initial structural domain  $\Omega$  which is transformed into a deformed (or perturbed) structural domain  $\Omega_\tau$  in a fictitious time  $\tau$ . This transformation can be viewed as a mapping  $\mathbf{T} : x \rightarrow x_\tau(x), x \in \Omega$  such that

$$\begin{aligned} x_\tau &\equiv \mathbf{T}(x, \tau) \\ \Omega_\tau &\equiv \mathbf{T}(\Omega, \tau) \end{aligned} \quad (33)$$

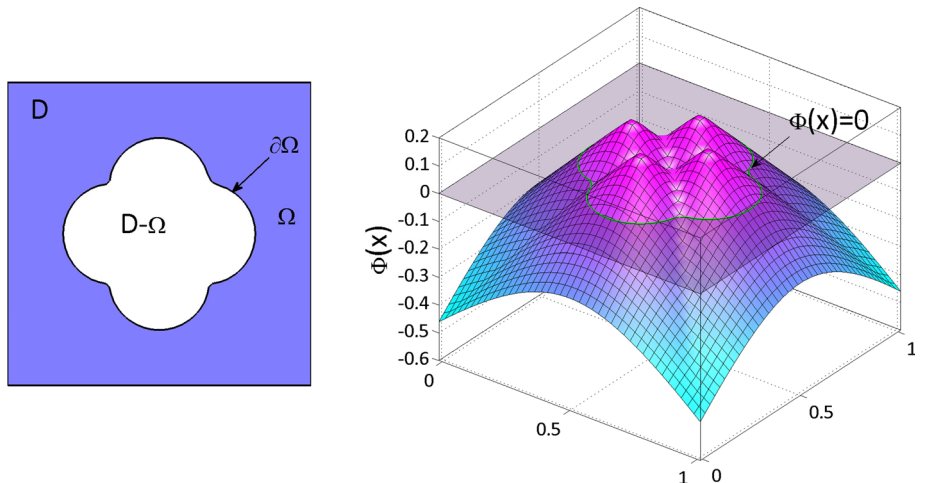
A design velocity field can be defined as

$$\mathbf{V}(x_\tau, \tau) \equiv \frac{dx_\tau}{d\tau} = \frac{d\mathbf{T}(x, \tau)}{d\tau} = \frac{\partial \mathbf{T}(x, \tau)}{\partial \tau} \quad (34)$$

Based on the linear Taylor's series expansion of  $\mathbf{T}(x, \tau)$  around  $\tau = 0$  [35], any material point in the initial domain

<sup>1</sup> This is the same as taking the material derivative of  $\{\Phi(\mathbf{x}(t), t) = 0\}$ .

**Fig. 1** Level set description of a plate with a hole. (left) Design domain (right) level set function



$x \in \Omega$  can be mapped onto a new material point in the perturbed domain  $x_\tau \in \Omega_\tau$  as

$$x_\tau(x) = \mathbf{T}(x, \tau) = x + \tau \mathbf{V}(x) \quad (35)$$

The material derivative of quantity  $z$  is defined as

$$\dot{z}(x) = \frac{d}{d\tau} z_\tau(x + \tau \mathbf{V}(x)) \Big|_{\tau=0} = z'(x) + \nabla z(x) \cdot \mathbf{V}(x) \quad (36)$$

where the over dot represents the material derivative and the prime denotes a local derivative.

**Lemma 1** Let  $\Psi_1$  be a domain functional defined as

$$\Psi_1 = \int_{\Omega_\tau} f_\tau(x_\tau) d\Omega_\tau$$

with  $f_\tau$  being a regular function defined in  $\Omega_\tau$ , then the material derivative of  $\Psi_1$  is given by

$$\begin{aligned} \dot{\Psi}_1 &= \int_{\Omega} [\dot{f}(x) + f(x)(\nabla \cdot \mathbf{V}(x))] d\Omega \\ &= \int_{\Omega} [f'(x) + \nabla \cdot (f(x)\mathbf{V}(x))] d\Omega \\ &= \int_{\Omega} f'(x) d\Omega + \int_{\Gamma} f(x)(\mathbf{V}(x) \cdot \mathbf{n}) d\Gamma \end{aligned}$$

**Lemma 2** Let  $\Psi_2$  be a boundary functional defined as

$$\Psi_2 = \int_{\Gamma_\tau} g_\tau(x_\tau) d\Gamma_\tau$$

with  $g_\tau$  being a regular function defined on  $\Gamma_\tau$ , then the material derivative of  $\Psi_2$  is given by

$$\begin{aligned} \dot{\Psi}_2 &= \int_{\Gamma} [\dot{g}(x) + \kappa g(x)(\mathbf{V}(x) \cdot \mathbf{n})] d\Gamma \\ &= \int_{\Gamma} [g'(x) + (\nabla g(x) \cdot \mathbf{n} + \kappa g(x))(\mathbf{V}(x) \cdot \mathbf{n})] d\Gamma \end{aligned}$$

where  $\kappa = \operatorname{div} \mathbf{n} = \nabla \cdot \mathbf{n}$  is the curvature of  $\Gamma$  in  $\mathbb{R}^2$  and twice the mean curvature of  $\Gamma$  in  $\mathbb{R}^3$ .

With these Lemmas [35] at hand, the material derivative of the objective functionals can be obtained as (see appendix 1 for details),

$$j_1 = \int_{\Omega} u' \cdot b d\Omega + \int_{\Gamma} u \cdot b V_n d\Gamma + \int_{\Gamma_N} (\nabla u \cdot t \cdot n + \kappa u \cdot t) V_n d\Gamma \quad (37)$$

$$\begin{aligned} j_2 &= c_0 \cdot \left( \int_{\Gamma} 2|u - u_0| u' d\Gamma + \int_{\Gamma} (\nabla(|u - u_0|^2)) \cdot n \right. \\ &\quad \left. + \kappa |u - u_0|^2 \right) V_n d\Gamma \quad (38) \end{aligned}$$

$$c_0 = \frac{1}{2} \left( \int_{\Gamma} |u - u_0|^2 d\Gamma \right)^{-\frac{1}{2}} \quad (39)$$

#### 4.2 Sensitivity analysis

In order to convert the constrained optimization problem to an unconstrained problem, an augmented objective functional  $L$  is constructed as

$$\begin{aligned} L &= J(\mathbf{u}, \Omega) + \chi(\Omega) \\ \chi(\Omega) &= \lambda \left( \int_{\Omega} d\Omega - \bar{V} \right) + \frac{1}{2\Lambda} \left( \int_{\Omega} d\Omega - \bar{V} \right)^2 \quad (40) \end{aligned}$$

in which  $\lambda$  is the Lagrange multiplier and  $\Lambda$  is a penalization parameter. These parameters are updated at each iteration  $k$  of the optimization process by the following rule

$$\begin{aligned}\lambda^{k+1} &= \lambda^k + \frac{1}{\Lambda^k} \left( \int_{\Omega} d\Omega - \bar{V} \right) \\ \Lambda^{k+1} &= \zeta \Lambda^k\end{aligned}\quad (41)$$

where  $\zeta \in (0, 1)$  is a constant parameter.

The shape derivative of augmented Lagrangian  $L$  is defined as

$$L' = J'(\mathbf{u}, \Omega) + \chi'(\Omega) \quad (42)$$

$$J' = \int_{\Gamma} G \cdot V_n d\Gamma \quad (43)$$

$$\begin{aligned}G &= - \int_{\Gamma} \boldsymbol{\epsilon}(\mathbf{u}) : \mathbb{C}^{bulk} : \boldsymbol{\epsilon}(\mathbf{w}) d\Gamma \\ &\quad - \int_{\Gamma} \kappa(\mathbf{P}\boldsymbol{\epsilon}(\mathbf{w})\mathbf{P} : \boldsymbol{\tau}_s) d\Gamma \\ &\quad - \int_{\Gamma} \kappa(\mathbf{P}\boldsymbol{\epsilon}(\mathbf{u})\mathbf{P} : \mathbb{C}^s : \mathbf{P}\boldsymbol{\epsilon}(\mathbf{w})\mathbf{P}) d\Gamma\end{aligned}\quad (44)$$

$$\chi'(\Omega) = \int_{\partial\Omega} \max \left\{ 0, \lambda + \frac{1}{\Lambda} \left( \int_{\Omega} d\Omega - \bar{V} \right) \right\} V_n d\Gamma \quad (45)$$

Based on the steepest descent direction,

$$\begin{aligned}V_n &= - \int_{\Gamma} \boldsymbol{\epsilon}(\mathbf{u}) : \mathbb{C}^{bulk} : \boldsymbol{\epsilon}(\mathbf{w}) d\Gamma \\ &\quad - \int_{\Gamma} \kappa(\mathbf{P}\boldsymbol{\epsilon}(\mathbf{w})\mathbf{P} : \boldsymbol{\tau}_s) d\Gamma \\ &\quad - \int_{\Gamma} \kappa(\mathbf{P}\boldsymbol{\epsilon}(\mathbf{u})\mathbf{P} : \mathbb{C}^s : \mathbf{P}\boldsymbol{\epsilon}(\mathbf{w})\mathbf{P}) d\Gamma\end{aligned}\quad (46)$$

$$J' = - \int_{\Gamma} V_n^2 d\Gamma \leq 0 \quad (47)$$

*Velocity extension* The normal velocity of the front  $V_n$  is to be extended from the front to the whole design domain in order to solve the HJ Eq. 25. Different techniques for velocity extension have been proposed in the literature e.g. the normal, natural, Hilbertian and Helmholtz velocity extension methods (see [36] for a review on different velocity extension strategies). It is obvious from Eq. 47 that the velocity comprises two parts, the bulk,  $V_b$  and surface terms,  $V_s$ . The bulk part of velocity,  $V_b$  can be obtained at each node whereas the surface part,  $V_s$  can be determined only along the surface. In order to solve HJ Eq. 25 that is posed throughout the domain, the surface part of velocity  $V_s$  is extended by extrapolation to the nodes that belong to the cut elements. The value of the speed function at the closest point on the surface is assigned

as the extension velocity to the nodal point [37], such that the condition  $V_{ext} = V_n$  at  $\phi = 0$  is satisfied.

## 5 Extended finite element method

XFEM is a robust numerical approach that enables modelling the evolution of discontinuities such as cracks without remeshing. It is used to analyze the nanobeams in each step of the iterative optimization process, where the XFEM formulation for solving nanomechanical boundary value problems including surface effects is based on the work of Farsad et al.[14]. In XFEM, the cracks, voids and material interfaces are implicitly represented by using level set functions [38, 39]. In XFEM, the approximation of the displacement field in a material with several material subdomains is given by

$$\mathbf{u}^h(\mathbf{X}) = \sum_{i \in I} N_i(\mathbf{X}) \mathbf{u}_i + \mathbf{u}^{enr} \quad (48)$$

$$\mathbf{u}^{enr} = \sum_{N=1}^{n_c} \sum_{j \in J} N_j(\mathbf{X}) \mathbf{a}_j^{(N)} F(\mathbf{X}) \quad (49)$$

where  $\mathbf{a}_j$  is the additional degrees of freedom (DOF) that accounts for the jump in the strain field,  $n_c$  denotes the number of material interfaces, and  $J$  is the set of all nodes whose support is cut by the material interface. In this work, the absolute enrichment function  $F(x)$  [40]

$$\mathbf{F}(\mathbf{X}) = \sum_I N_i(\mathbf{X}) |\phi_i(\mathbf{X})| - |N_i(x)\phi_i(\mathbf{X})| \quad (50)$$

is used in order to account for the discontinuous strain field along  $\Gamma$ . The voids are assumed to be filled with a material that is 1000 times softer than the stiffness of the nanostructure. The usage of a softer material enables the traction and displacement boundary to intersect with the void boundary. The stiffness coefficients are determined by numerical integration performed over sub triangles on either side of the inclusion interface. Substituting the displacement field in Eq. 48 to the weak formulation, Eq. 18, the algebraic finite element equations can be obtained. The expressions for  $a(\mathbf{u}, \delta\mathbf{u})$ ,  $a_s(\mathbf{u}, \delta\mathbf{u})$ ,  $l_s(\delta\mathbf{u})$  and  $l(\delta\mathbf{u})$  for an element can be rewritten using the FE approximation as,

$$a^e(\mathbf{u}, \delta\mathbf{u}) = \delta\mathbf{u}^e T \left( \int_{\Omega^e} \mathbf{B}^T \{ \mathbb{C}^{bulk} \} \mathbf{B} d\Omega^e \right) \mathbf{u}^e \quad (51)$$

$$a_s^e(\mathbf{u}, \delta\mathbf{u}) + l_s^e(\delta\mathbf{u}) = \int_{\Gamma^e} (\mathbf{P}\boldsymbol{\epsilon}(\mathbf{u})\mathbf{P}) \{ \mathbb{C}^s \} (\mathbf{P}\boldsymbol{\epsilon}(\delta\mathbf{u})\mathbf{P}) d\Gamma^e$$

$$\begin{aligned}
& + \int_{\Gamma^e} \tau_s (\mathbf{P}\epsilon(\mathbf{u})\mathbf{P}) d\Gamma^e \\
& = \delta \mathbf{u}^{\epsilon T} \left( \int_{\Gamma^e} \mathbf{B}^T \mathbf{M}_{pT} \{C^s\} \mathbf{M}_p \mathbf{B} d\Gamma^e \right) \mathbf{u}^\epsilon \\
& + \delta \mathbf{u}^{\epsilon T} \int_{\Gamma^e} \mathbf{B}^T \mathbf{M}_{pT} \tau_s d\Gamma^e \quad (52)
\end{aligned}$$

$$l^e(\delta \mathbf{u}) = \delta \mathbf{u}^{\epsilon T} \left( \int_{\Gamma_N^e} \mathbf{N}^T \bar{\mathbf{t}} d\Gamma^e + \int_{\Omega} \mathbf{N}^T \mathbf{b} d\Omega^e \right) \quad (53)$$

where  $\mathbf{u} \in H^1(\Omega)$  and  $\delta \mathbf{u} \in H^1(\Omega)$ .

The final system of discrete algebraic XFEM equations is,

$$(\mathbf{K}_b + \mathbf{K}_s)\mathbf{u} = -\mathbf{f}_s + \mathbf{f}_{ext} \quad (54)$$

$$\mathbf{K}_b = \int_{\Omega} \mathbf{B}^T \{C^{bulk}\} \mathbf{B} d\Omega$$

$$\mathbf{K}_s = \int_{\Gamma} \mathbf{B}^T \mathbf{M}_p^T \cdot \{C^s\} \cdot \mathbf{M}_p \mathbf{B} d\Gamma$$

$$\mathbf{f}_s = \int_{\Gamma} \mathbf{B}^T \cdot \mathbf{M}_p^T \tau_s d\Gamma$$

$$\mathbf{f}_{ext} = \int_{\Gamma_N} \mathbf{N}^T \bar{\mathbf{t}} d\Gamma + \int_{\Omega} \mathbf{N}^T \mathbf{b} d\Omega \quad (55)$$

where  $K_s$  is the surface stiffness matrix, while  $f_s$  is the surface residual.  $M_p$  and  $C^s$  are defined as [14],

$$M_p = \begin{pmatrix} P_{11}^2 & P_{12}^2 & P_{11}P_{12} \\ P_{12}^2 & P_{22}^2 & P_{12}P_{22} \\ 2P_{11}P_{12} & 2P_{12}P_{22} & P_{12}^2 + P_{11}P_{22} \end{pmatrix} \quad (56)$$

$$C^s = M_p^T S^s M_p \quad (57)$$

$$S^s = \begin{pmatrix} S_{1111} & S_{1122} & 0 \\ S_{1122} & S_{2222} & 0 \\ 0 & 0 & S_{1212} \end{pmatrix} \quad (58)$$

The steps involved in the process of optimizing nano structures using XFEM and level set coupled methodology is shown as a flowchart in Fig. 2.

## 6 Numerical examples

In this section, several examples are solved to determine the influence of surface effects on the optimum topology of nanostructures, and specifically, nanobeams. Our choice of nanobeams is driven by multiple reasons. First, nanobeams are the basic functional element in most nanoelectromechanical systems (NEMS) [41–43]. Second, the

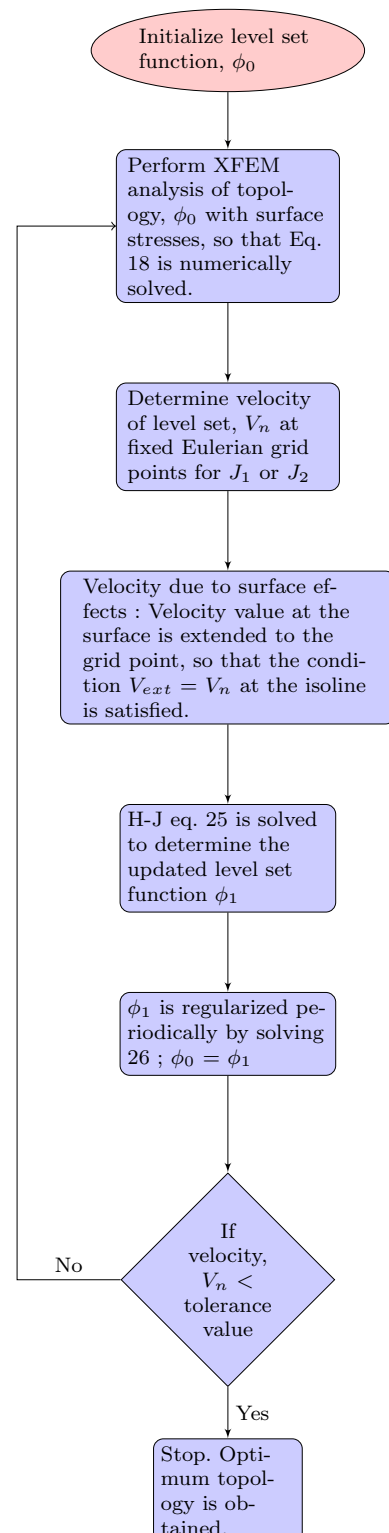


**Fig. 2** Flowchart showing steps involved in the process of optimizing nano structures with surface effects

topology optimization of beams has been widely studied in the literature, and as a result, it would be interesting to examine how surface effects alter the optimal topologies of

**Table 1**  $E$  (bulk Youngs modulus),  $\nu$  (Poisson ratio) and  $S_{ijkl}$  (surface stiffness) for Gold (Au) from atomistic calculations [44]

$E$ (GPa)	$\nu$	$S_{1111} = S_{2222}$ (J/m <sup>2</sup> )
36	0.44	5.26
$S_{1122} = S_{2211}$ (J/m <sup>2</sup> )	$S_{1212}$ (J/m <sup>2</sup> )	$\tau^0$ (J/m <sup>2</sup> )
2.53	3.95	1.57

nanobeams when surface effects are accounted for. Manufacturability of the optimal topologies may be an issue with regards to the smallest nanobeams we have optimized in this work.

The topology optimization is performed for two different beams, i.e. cantilever and fixed beam. The objective functions discussed in Sect. 4 are employed, i.e. minimum total potential energy and minimum least square error compared to a target displacement. The nanobeam is assumed to be made of gold, where the bulk and surface properties are given in Table 1. For the XFEM analysis, the domain is discretized by using bilinear quadrilateral (Q4) elements.

In the following numerical examples, the velocity of the level set function,  $V_n$  is evaluated at all node points, so as to solve the HJ equation throughout the domain. From Eq. 47, it can be seen that it also includes surface terms which are available only along the interface. The surface terms are extrapolated to nodes of those elements which are cut by the interface, while these terms are neglected at all other nodal locations.

A short cantilever beam of size 32X20 units subjected to a point load at the free end is optimized using the LSM. The optimum topology for a volume ratio of 0.4 is shown in Fig. 3b. The optimum topology is similar to the one shown in [46], obtained by SIMP.

In order to obtain best results using conventional LSM, the optimization process is initialized with sufficiently large number of voids that are uniformly distributed all over the domain [47] as shown in Fig. 3a.

## 6.1 Cantilever beam

### 6.1.1 Objective function $J_1$

In this section, optimization of nanobeams subject to cantilever boundary conditions is performed such that total potential energy is minimized. The first geometry is an 80 × 20 nm nanobeam that is optimized for minimum total potential energy. The load applied at the free end is a point load of magnitude 3.6 nN, while the volume ratio, which is defined as the ratio of volume of the optimized beam to the initial volume, is restricted to 70 %. The optimum topology with a mesh of 120 × 30 bilinear quadrilateral elements is

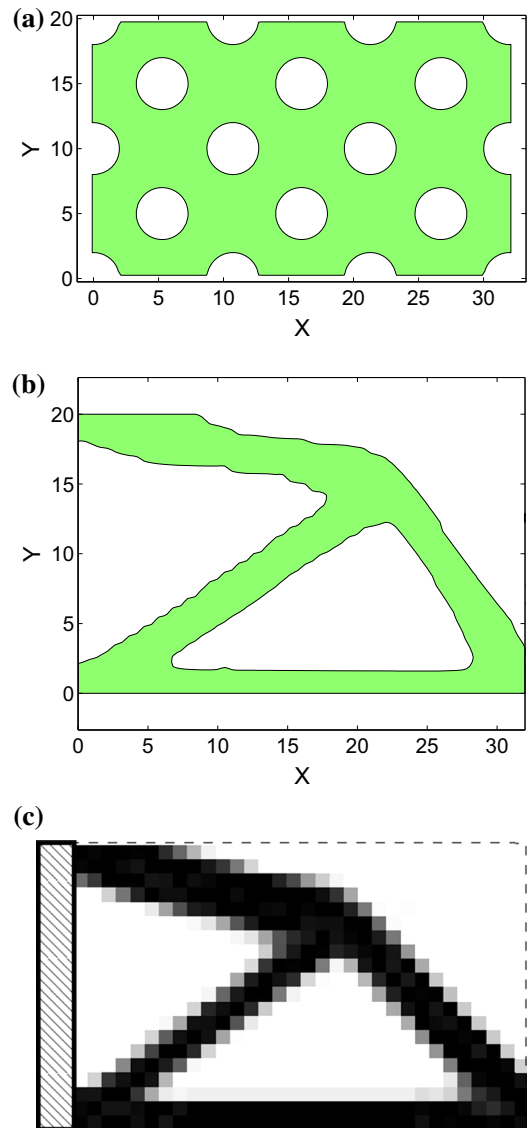


**Fig. 3** **a** Initialization **b** optimum topology for a short cantilever beam subjected to a point load at free end by Level set method **(c)** by SIMP [46]

shown in Fig. 4a. The optimization process is then repeated by neglecting surface effects, i.e. taking  $C_s = 0$  and  $\tau_s = 0$ , with the result seen in Fig. 4b.

It is evident from the optimum topologies shown in Fig. 4 that surface effects do not influence the optimum topology for the minimum energy objective function. This occurs through the stiffness ratio, which is defined as the ratio between the difference in vertical displacement at the load location with and without surface effects, and the vertical displacement at the load location with surface effects, is about 4.25 %.

Besides the thickness, the aspect ratio is known to have an important effect on the mechanical properties of nano beams [7, 45], and thus we consider a nanobeam with dimen-

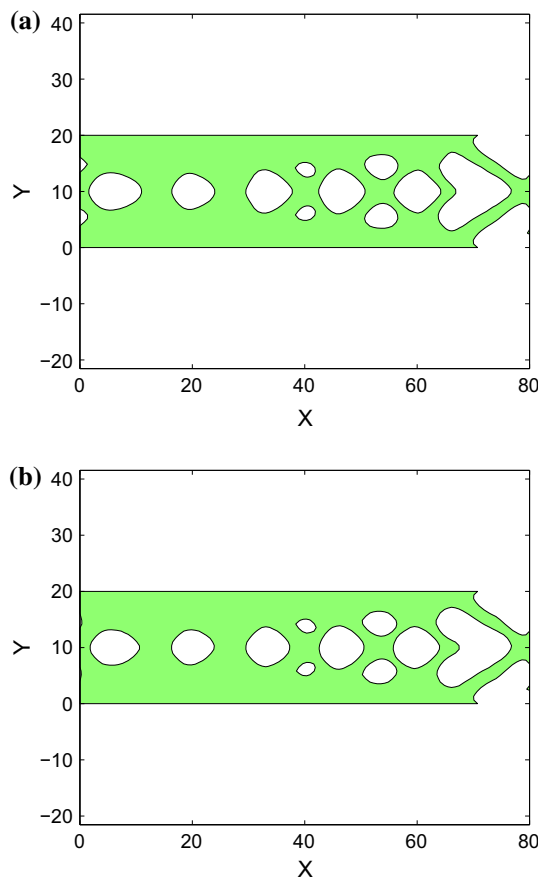


**Fig. 4** Optimal topology for  $80 \times 20$  nm cantilever nano beam for objective function  $J_1$  **a** with surface effects , **b** without surface effects, i.e. taking  $C_s$  and  $\tau_s$  to be zero

sions of  $200 \times 20$  nm, for an aspect ratio of 10. The stiffness ratio of this beam is found to be 4.35 %, while the volume ratio is again constrained to 70 %. Again, no noticeable differences for the  $J_1$  objective function was observed even when surface effects are accounted for.

The main reason why little difference is observed between the optimal topologies with and without surface effects in Figs. 4 and 5 is due to the fact that the volume constraint is the same for both problems. As will be shown in the subsequent examples with the  $J_2$  objective function, for that objective function the volume fraction is allowed to vary. This will prove to be key in allowing surface effects to change the optimal design as less material is needed due to the stiffening that is induced by surface effects [5, 14].

### 6.1.2 Objective function $J_2$

We now consider a different objective function, i.e. the minimization of the least square error objective function, for the cantilever nanobeam.

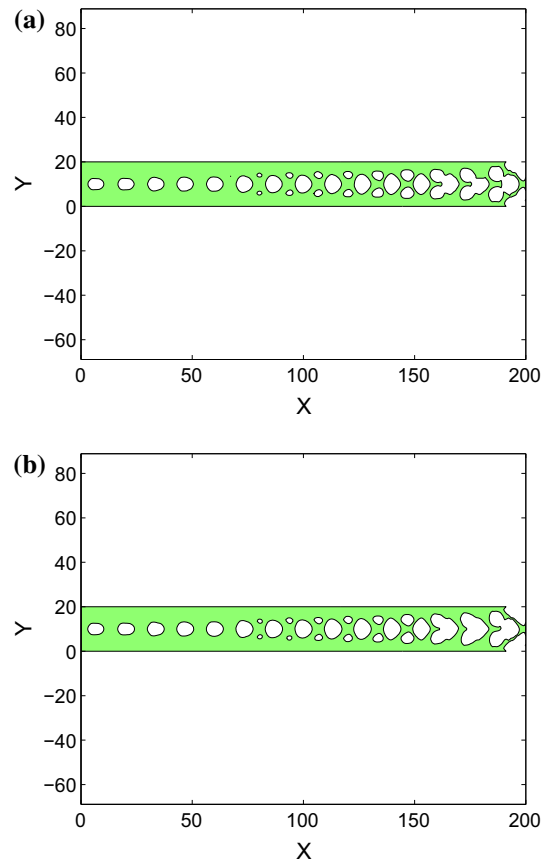


**Fig. 5** Optimal topology for  $200 \times 20$  nm cantilever nano beam for objective function  $J_1$  **a** with surface effects , **b** without surface effects, i.e. taking  $C_s$  and  $\tau_s$  to be zero

A cantilever nanobeam of size  $40 \times 10$  nm is subjected to a point load of 3.6 nN at the free ( $40, 0$ ) nm end. The target displacement at the load location is 16 nm. The optimum topology obtained is shown in Fig. 6, where the volume ratio of the optimum topology is 0.59 and the stiffness ratio of the  $40 \times 10$  nm beam is 8.6 %.

Now the aspect ratio is maintained as 4 and the thickness of the beam is increased. Thus, Fig. 6 shows the optimum shape obtained for beam of size  $320 \times 80$  nm, which have stiffness ratios of 1.05 %, and volume ratio of 0.71.

The optimum topology obtained for the  $320 \times 80$  nm beam with and without surface effects appear similar, which suggests that for this particular aspect ratio and objective function, surface effects lose their effect once the nanobeam thickness is larger than about 80 nm. However, the 10 nm thick nanobeam have different optimal designs, which is driven by the fact that the smaller nanostructures are stiffer [6] as demonstrated by the stiffness ratios, and thus require less material to conform to the maximum displacement constraint.

The intermediate topologies obtained at various iteration steps are shown in Fig. 7, for the optimization of the  $40 \times 10$

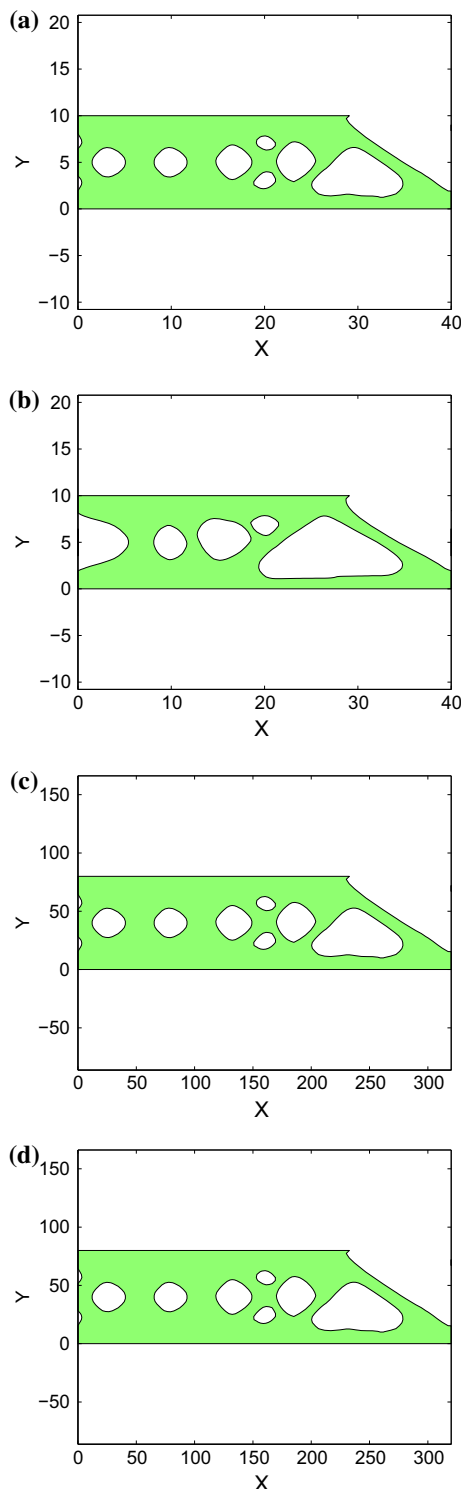


**Fig. 6** The optimal topology obtained for  $J_2$  objective function for  $40 \times 10$  nm and  $320 \times 80$  nm cantilever beams without surface effects (a), (c) and with surface effects (b), (d)

cantilever nano beam with surface effects. The convergence of the optimization process with decrease in mesh size is shown in Fig. 8. It is evident from the figure that volume ratio

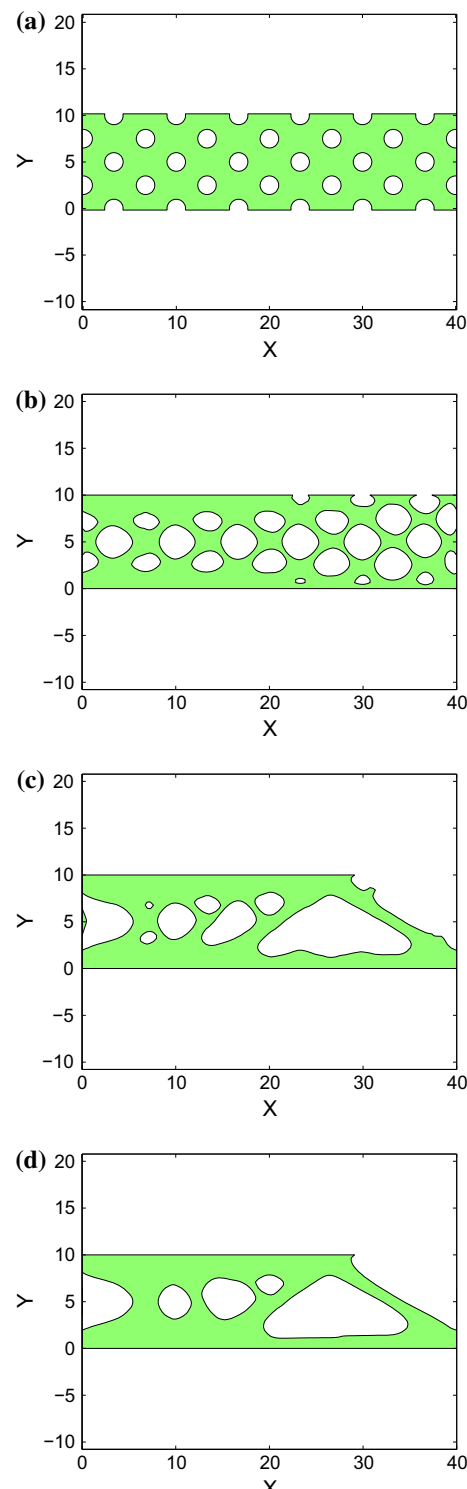


**Fig. 7** Intermediate topologies for optimization of objective function  $J_2$  for  $40 \times 10$  nm cantilever nanobeam with surface effects at iteration a 1, b 15, c 35, d 75, e 200

of the optimum topology converges for a mesh size smaller than  $120 \times 30$  (i.e.)  $h = \frac{1}{3}$  for the problem solved in this example. The optimum topology obtained for three different

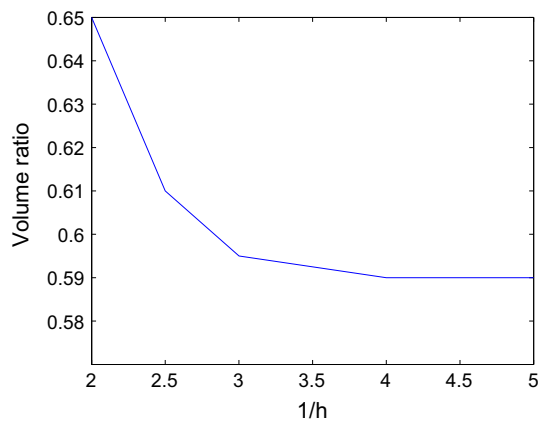


**Fig. 8** Convergence of Volume ratio, for objective function  $J_2$  with iterations

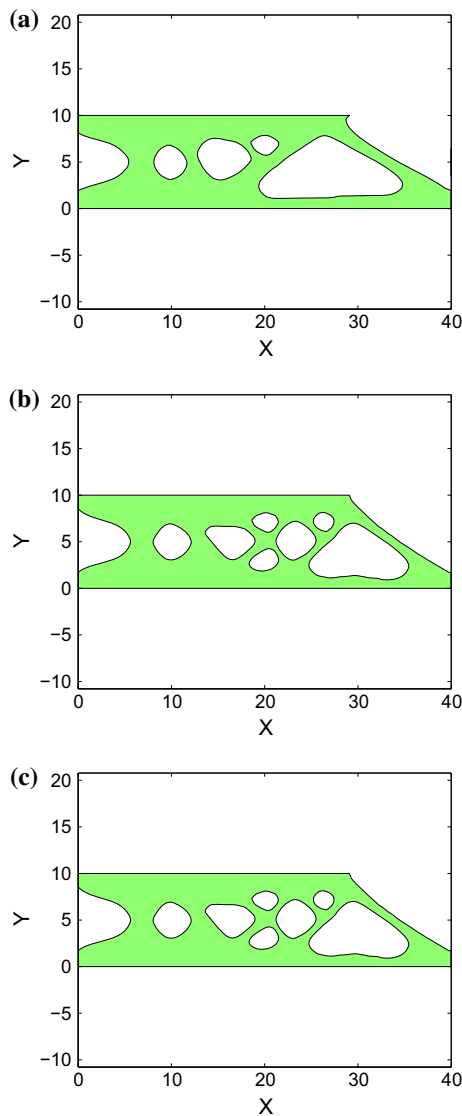


**Fig. 9** Optimal topology for objective function  $J_2$  for 40x10 nm cantilever nanobeam with surface effects for mesh sizes **a** 120x30 **b** 160x40 and **c** 180x45

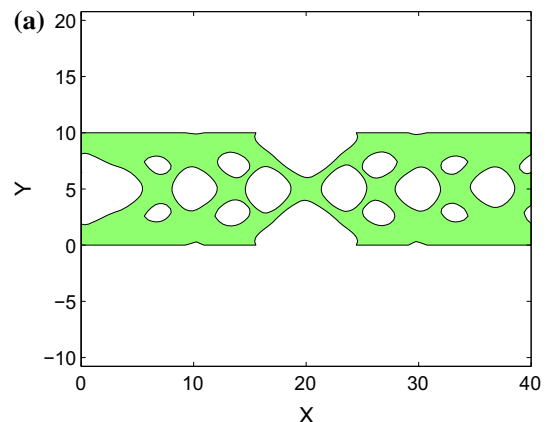


**Fig. 10** Optimal topology for objective function  $J_1$  for 80x10 nm fixed nanobeam **a** with surface effects, **b** without surface effects, i.e. taking  $C_s$  and  $\tau_s$  to be zero

mesh sizes  $120 \times 30$ ,  $160 \times 40$  and  $180 \times 45$  are shown in the Fig. 9.

## 6.2 Fixed beam

### 6.2.1 Objective function $J_1$

We now consider a nanobeam with fixed boundary conditions subject to both objective functions. For the minimum potential energy ( $J_1$ ) constraint, we first consider a fixed nanobeam of dimensions  $80 \times 10$  nm. A load of 3.6 nN is applied at the midpoint and the volume ratio is constrained to 70 %. We exploit the symmetry boundary conditions and thus model only half of the nanobeam. The stiffness ratio of the  $80 \times 10$  nm nanobeam is found to be 6.9 %, and the optimum topology both with and without surface effects is shown in Fig. 10, where again only slight differences are observed for the structure including surface effects.

We also consider larger aspect ratio nanobeam of dimensions  $200 \times 10$  nm, which leads to a stiffness ratio of 8.4 %, while the volume ratio was constrained to be 70 %. The

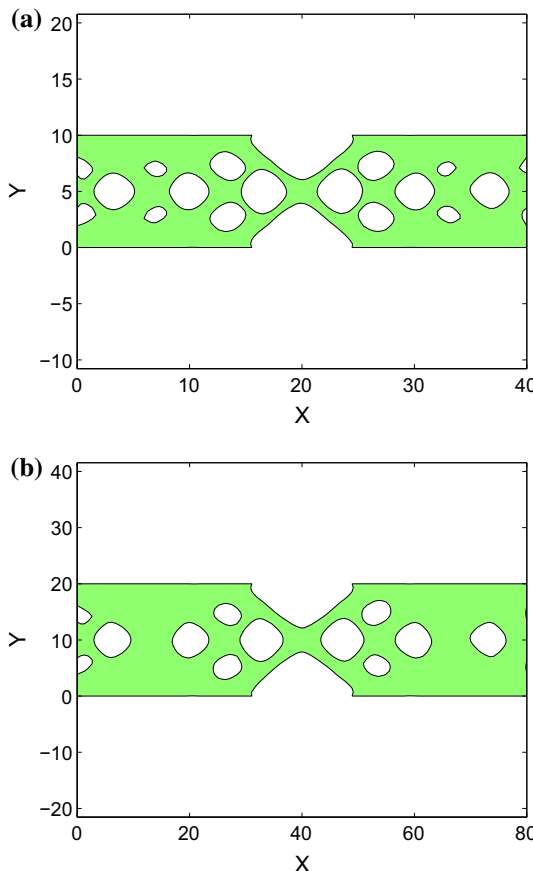


**Fig. 11** Optimal topology for objective function  $J_2$  for **a**  $80 \times 10$  nm and **b**  $160 \times 20$  nm fixed nanobeam

topologies obtained do not change for the  $J_1$  objective function with inclusion of surface effects even for an increased nanobeam aspect ratio.

#### 6.2.2 Objective function $J_2$

We next consider the optimal design of a fixed nanobeam subjected to the  $J_2$  objective function. The  $80 \times 10$  nm fixed nanobeam is subjected, as for the  $J_1$  case above, to a point load of 3.6 nN at the midspan where the displacement at the load location is restricted to 4.7 nm, and where again exploiting symmetry only half of the beam is modeled.

The optimum topology obtained is shown in Fig. 11a, where the volume ratio of the optimum topology is 0.65. The optimization process is again repeated by increasing the dimension to  $160 \times 20$  nm in Fig. 11b, which thus keeps the aspect ratio constant at 8. The volume ratio of 0.71 for the larger nanobeam is higher than that of the  $80 \times 10$  beam due to reduced stiffness that occurs for larger nanobeam sizes [14, 22], which enables the nanobeam in Fig. 11a to have more voids while still allowing only the maximal displacement at the load location.

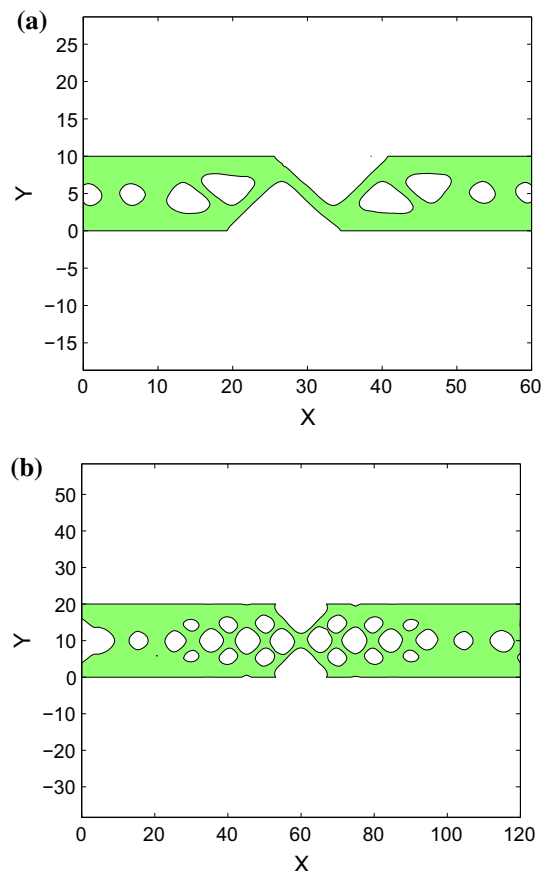


**Fig. 12** Optimal topology for objective function  $J_2$  for **a**  $120 \times 10$  nm and **b**  $240 \times 20$  nm fixed nanobeam

While Fig. 11 shows the optimal design for an aspect ratio of 8, Fig. 12 shows the optimal design when the aspect ratio is increased to 12, for nanobeam thicknesses of 10 and 20 nm, and when the displacement at the load location is restricted to 12 nm. The volume ratio of the optimum topology is 0.65 for the 10 nm thick nanobeam, and 0.7 for the 20 nm thick nanobeam. It is evident from Fig. 12 that increasing the aspect ratio causes the surface effects to play a strong role in influencing the optimal design of the fixed nanobeams.

The stiffness ratios for  $80 \times 10$  nm and  $120 \times 10$  nm are 6.9 and 7.9 % respectively. The stiffness ratios increase with increase in length of the fixed beam until the beam length reaches 320 nm (at a constant depth of 10 nm) after which they gradually start decreasing. A stiffness ratio of around 8 % or more leads to significant difference in optimum topology in a fixed nano beam compared to a micro/macro fixed beam subjected to point load at mid span for objective function  $J_2$ .

Different initializations are tried and the optimum topology shown in Fig. 12a, is the one with least volume ratios among the optimum topologies obtained. The initializations

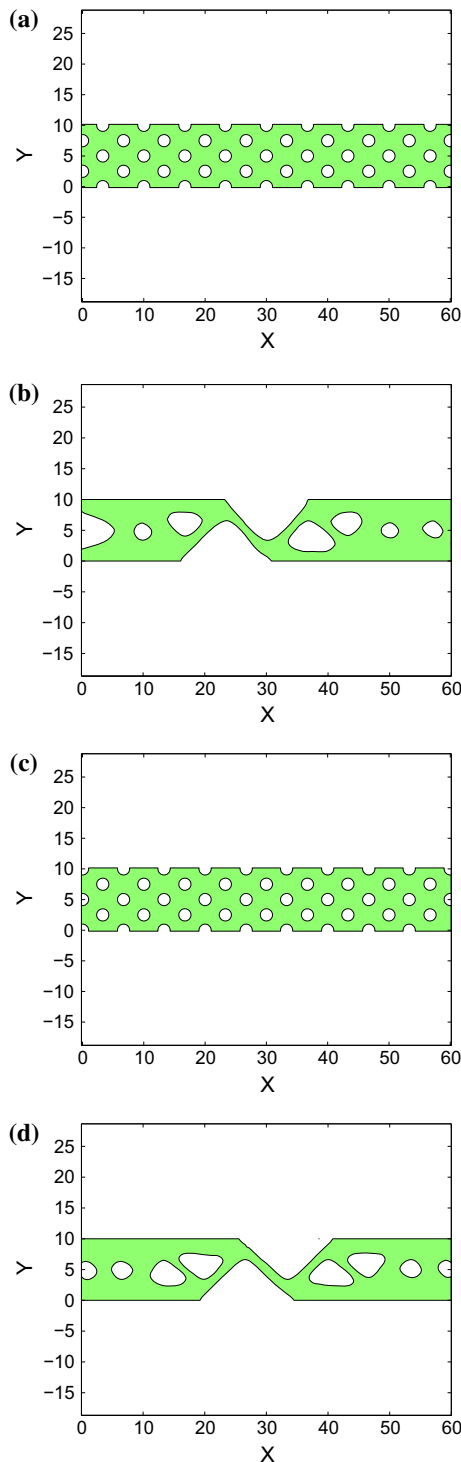


**Fig. 13** Initialization **a**, **c** and their corresponding Optimal topologies **b**, **d** for objective function  $J_2$  for  $120 \times 10 \text{ nm}$

and the corresponding optimum topologies are shown in Fig. 13.

## 7 Conclusion

We have presented a coupled XFEM/level set methodology to perform shape and topology optimization of nanostructures while accounting for nanoscale surface effects. The new formulation was used in conjunction with two objective functions, those of minimum potential energy and least square error in the targeted displacement. While surface effects did not impact the optimized structure for the minimum potential energy objective function, substantial size and aspect ratio effects were observed for the least square displacement error objective function. These arise due to the change in volume and stiffness ratios. Thus optimum topologies are influenced by the size-dependent stiffening of nanostructures that occurs with decreasing size as a result of the surface effects. Overall, the methodology presented here should enable new insights and approaches to designing and engineering the behavior and performance of nanoscale structural elements.

There are many opportunities for future work. For example, due to the ubiquitous nature of nanobeams in NEMS, work could be done to optimize geometries to produce a desired resonant frequency. Opportunities also exist to pursue the optimization of nanobeams where the coupling of physics, i.e. electrical and mechanical, are of interest. Work in this respect is already underway.

**Acknowledgments** Timon Rabczuk and Navid Valizadeh gratefully acknowledge the financial support of the Framework Programme 7 Initial Training Network Funding under grant number 289361 “Integrating Numerical Simulation and Geometric Design Technology”. Harold Park acknowledges the support of the Mechanical Engineering department at Boston University. S. S. Nanthakumar gratefully acknowledges the financial support of DAAD.

## Appendix: Derivation of shape derivative

Firstly, the total potential energy objective function is considered. The objective function and its constraints are as follows,

$$\text{Minimize } J(\Omega) = \int_{\Omega} \mathbf{u} \cdot \mathbf{b} \, d\Omega + \int_{\Gamma_N} \mathbf{u} \cdot \mathbf{t} \, d\Gamma$$

subject to :

$$a(\mathbf{u}, \delta\mathbf{u}, \Omega) + a_s(\mathbf{u}, \delta\mathbf{u}, \Omega) = -l_s(\mathbf{u}, \Omega) + l(\mathbf{u}, \Omega)$$

(i.e.)

$$\begin{aligned} \int_{\Omega} \boldsymbol{\epsilon}(\delta\mathbf{u}) : \mathbb{C}^{\text{bulk}} : \boldsymbol{\epsilon}(\mathbf{u}) \, d\Omega + \int_{\Gamma} (\mathbf{P}\boldsymbol{\epsilon}(\delta\mathbf{u})\mathbf{P}) : \boldsymbol{\tau}_s \, d\Gamma + \\ \int_{\Gamma} (\mathbf{P}\boldsymbol{\epsilon}(\delta\mathbf{u})\mathbf{P}) : \mathbb{C}^s : (\mathbf{P}\boldsymbol{\epsilon}(\mathbf{u})\mathbf{P}) \, d\Gamma = \int_{\Omega} \mathbf{u} \cdot \mathbf{b} \, d\Omega + \int_{\Gamma} \mathbf{u} \cdot \mathbf{t} \, d\Gamma. \end{aligned}$$

$$\begin{aligned} \dot{a}(\mathbf{u}, \mathbf{w}, \Omega) + \dot{a}_s(\mathbf{u}, \mathbf{w}, \Omega) + \dot{l}_s(\mathbf{w}, \Omega) \\ = \int_{\Omega} \boldsymbol{\epsilon}(\mathbf{u}') : \mathbb{C}^{\text{bulk}} : \boldsymbol{\epsilon}(\mathbf{w}) \, d\Omega + \int_{\Omega} \boldsymbol{\epsilon}(\mathbf{u}) : \mathbb{C}^{\text{bulk}} : \boldsymbol{\epsilon}(\mathbf{w}') \, d\Omega \\ + \int_{\Gamma} \boldsymbol{\epsilon}(\mathbf{u}) : \mathbb{C}^{\text{bulk}} : \boldsymbol{\epsilon}(\mathbf{w}) V_n \, d\Gamma \end{aligned}$$

$$\begin{aligned}
& + \int_{\Gamma} \mathbf{P}\epsilon(\mathbf{w}')\mathbf{P} : \boldsymbol{\tau}_s d\Gamma + \int_{\Gamma} (\nabla_s(\mathbf{P}\epsilon(\mathbf{w})\mathbf{P} : \boldsymbol{\tau}_s) \cdot \mathbf{n} \\
& + \kappa(\mathbf{P}\epsilon(\mathbf{w})\mathbf{P} : \boldsymbol{\tau}_s)) V_n d\Gamma \\
& + \int_{\Gamma} (\mathbf{P}\epsilon(\mathbf{u}')\mathbf{P}) : \mathbb{C}^s : (\mathbf{P}\epsilon(\mathbf{w})\mathbf{P}) d\Gamma \\
& + \int_{\Gamma} (\mathbf{P}\epsilon(\mathbf{u})\mathbf{P}) : \mathbb{C}^s : (\mathbf{P}\epsilon(\mathbf{w}')\mathbf{P}) d\Gamma \\
& + \int_{\Gamma} (\nabla_s(\mathbf{P}\epsilon(\mathbf{u})\mathbf{P}) : \mathbb{C}^s : (\mathbf{P}\epsilon(\mathbf{w})\mathbf{P}) \cdot \mathbf{n} V_n d\Gamma \\
& + \int_{\Gamma} (\mathbf{P}\epsilon(\mathbf{u})\mathbf{P}) : \mathbb{C}^s : \nabla_s(\mathbf{P}\epsilon(\mathbf{w})\mathbf{P}) \cdot \mathbf{n} V_n d\Gamma \\
& \int_{\Gamma} \kappa(\mathbf{P}\epsilon(\mathbf{u})\mathbf{P} : \mathbb{C}^s : \mathbf{P}\epsilon(\mathbf{w})\mathbf{P}) V_n d\Gamma. \tag{59}
\end{aligned}$$

$$\begin{aligned}
l(\mathbf{w}, \Omega) &= \int_{\Omega} \mathbf{w}' \cdot \mathbf{b} d\Omega + \int_{\Gamma} \mathbf{w} \cdot \mathbf{b} V_n d\Gamma + \int_{\Gamma_N} \mathbf{w}' \cdot \mathbf{t} d\Gamma \\
& + \int_{\Gamma_N} (\nabla(\mathbf{w} \cdot \mathbf{t}) \cdot \mathbf{n} + \kappa \mathbf{w} \cdot \mathbf{t}) V_n d\Gamma \tag{60}
\end{aligned}$$

$$j = \int_{\Omega} \mathbf{u}' \cdot \mathbf{b} d\Omega + \int_{\Gamma} \mathbf{u} \cdot \mathbf{b} V_n d\Gamma + \int_{\Gamma_N} (\nabla(\mathbf{u} \cdot \mathbf{t}) \cdot \mathbf{n} + \kappa \mathbf{u} \cdot \mathbf{t}) V_n d\Gamma. \tag{61}$$

The Lagrangian of the objective functional is,

$$\begin{aligned}
L &= J + l(\mathbf{w}, \Omega) - a(\mathbf{u}, \mathbf{w}, \Omega) - a_s(\mathbf{u}, \mathbf{w}, \Omega) \\
& - l_s(\mathbf{w}, \Omega). \tag{62}
\end{aligned}$$

The material derivative of the Lagrangian is defined as ,

$$\begin{aligned}
\dot{L} &= j + l(\mathbf{w}, \Omega) - \dot{a}(\mathbf{u}, \mathbf{w}, \Omega) \\
& - \dot{a}_s(\mathbf{u}, \mathbf{w}, \Omega) - \dot{l}_s(\mathbf{w}, \Omega). \tag{63}
\end{aligned}$$

All the terms that contain  $\mathbf{w}'$  in the material derivative of Lagrangian are collected and the sum of these terms is set to zero, to get the weak form of the state equation,

$$\begin{aligned}
& \int_{\Omega} \mathbf{w}' \cdot \mathbf{b} d\Omega + \int_{\Gamma_N} \mathbf{w}' \cdot \mathbf{t} d\Gamma = \int_{\Omega} \epsilon(\mathbf{u}) : \mathbb{C}^{bulk} : \epsilon(\mathbf{w}') d\Omega \\
& + \int_{\Gamma} \mathbf{P}\epsilon(\mathbf{w}')\mathbf{P} : \boldsymbol{\tau}_s d\Gamma + \int_{\Gamma} (\mathbf{P}\epsilon(\mathbf{u})\mathbf{P} : \mathbb{C}^s : \mathbf{P}\epsilon(\mathbf{w}')\mathbf{P}) d\Gamma. \tag{64}
\end{aligned}$$

All the terms that contain  $\mathbf{u}'$  in the material derivative of Lagrangian are collected and the sum of these terms is set to

zero, to get the weak form of the adjoint equation,

$$\begin{aligned}
& \int_{\Omega} \mathbf{u}' \cdot \mathbf{b} d\Omega + \int_{\Gamma_N} \mathbf{u}' \cdot \mathbf{t} d\Gamma = \int_{\Omega} \epsilon(\mathbf{u}') : \mathbb{C}^{bulk} : \epsilon(\mathbf{w}) d\Omega \\
& + \int_{\Gamma} (\mathbf{P}\epsilon(\mathbf{u}')\mathbf{P} : \mathbb{C}^s : \mathbf{P}\epsilon(\mathbf{w})\mathbf{P}) d\Gamma. \tag{65}
\end{aligned}$$

Considering that  $\Gamma_N$  and  $\Gamma_D$  are not modified in the optimization process and assuming that the body forces are zero, the shape derivative of the objective functional can be obtained from Eq. 63,

$$J' = \int_{\Gamma_H} G \cdot V_n d\Gamma \tag{66}$$

where,

$$\begin{aligned}
G &= - \int_{\Gamma} \epsilon(\mathbf{u}) : \mathbb{C}^{bulk} : \epsilon(\mathbf{w}) d\Gamma \\
& - \int_{\Omega} \kappa(\mathbf{P}\epsilon(\mathbf{w})\mathbf{P} : \boldsymbol{\tau}_s) d\Gamma \\
& - \int_{\Gamma} \kappa(\mathbf{P}\epsilon(\mathbf{u})\mathbf{P} : \mathbb{C}^s : \mathbf{P}\epsilon(\mathbf{w})\mathbf{P}) d\Gamma \tag{67}
\end{aligned}$$

The  $G$  obtained can be considered as the negative of velocity,  $V_n$  required in order to optimize the level set function. Therefore,

$$J' = - \int_{\Gamma_H} \mathbf{G}^2 d\Gamma. \tag{68}$$

From the above equation it is evident that the derivative is negative (i.e.) it ensures decrease in the objective function with iterations.

If the objective function is a least square error compared to target displacement as shown below,

$$J(\Omega) = \left( \int_{\Gamma_N} |\mathbf{u} - \mathbf{u}_0|^2 d\Gamma \right)^{\frac{1}{2}} \tag{69}$$

$$\begin{aligned}
J &= c_0 \cdot \left( \int_{\Gamma_N} 2|\mathbf{u} - \mathbf{u}_0| \mathbf{u}' d\Gamma + \int_{\Gamma_N} (\nabla(|\mathbf{u} - \mathbf{u}_0|^2)) \cdot \mathbf{n} \right. \\
& \left. + \kappa |\mathbf{u} - \mathbf{u}_0|^2 \right) V_n d\Gamma. \tag{70}
\end{aligned}$$

Substituting in Eq. 63 and collecting terms with  $\mathbf{u}'$ , the weak form of the adjoint can be obtained as,

$$\begin{aligned} c_0 \int_{\Gamma_N} 2|\mathbf{u} - \mathbf{u}_0| \mathbf{u}' d\Gamma &= \int_{\Omega} \boldsymbol{\epsilon}(\mathbf{u}') \mathbb{C}^{bulk} \boldsymbol{\epsilon}(\mathbf{w}) d\Omega \\ &\quad + \int_{\Gamma} (\mathbf{P}\boldsymbol{\epsilon}(\mathbf{u}')\mathbf{P} : \mathbb{C}^s : \mathbf{P}\boldsymbol{\epsilon}(\mathbf{w})\mathbf{P}) d\Gamma \end{aligned} \quad (71)$$

where,

$$c_0 = \frac{1}{2} \left( \int_{\Gamma_N} |\mathbf{u} - \mathbf{u}_0|^2 d\Gamma \right)^{-\frac{1}{2}} \quad (72)$$

## References

- Xia Y, Yang P, Sun Y, Wu Y, Mayers B, Gates B, Yin Y, Kim F, Yan H (2003) One-dimensional nanostructures:synthesis, characterization, and applications. *Adv Mater* 15(5):353–389
- Lieber CM, Wang ZL (2007) Functional nanowires. *MRS Bull* 32:99–108
- Haiss W (2001) Surface stress of clean and adsorbate-covered solids. *Rep Prog Phys* 64:591–648
- Cammarata RC (1994) Surface and interface stress effects in thin films. *Prog Surf Sci* 46(1):1–38
- Zhou LG, Huang H (2004) Are surfaces elastically softer or stiffer? *Appl Phys Lett* 84(11):1940–1942
- Park HS, Cai W, Espinosa HD, Huang H (2009) Mechanics of crystalline nanowires. *MRS Bull* 34(3):178–183
- Park HS, Gall K, Zimmerman JA (2006) Deformation of FCC nanowires by twinning and slip. *J Mech Phys Solids* 54(9):1862–1881
- Park HS, Gall K, Zimmerman JA (2005) Shape memory and pseudoelasticity in metal nanowires. *Phys Rev Lett* 95:255504
- Liang W, Zhou M, Ke F (2005) Shape memory effect in Cu nanowires. *Nano Lett* 5(10):2039–2043
- Weinberger CR, Cai W (2012) Plasticity of metal nano wires. *J Mater Chem* 22(8):3277–3292
- Yvonnet J, Quang HL, He QC (2008) An XFEM/level set approach to modelling surface/interface effects and to computing the size-dependent effective properties of nanocomposites. *Comput Mech* 42:119–131
- Yvonnet J, Mitrushchenkov A, Chambaud G, He GC (2011) Finite element model of ionic nanowires with size-dependent mechanical properties determined by ab initio calculations. *Comput Methods Appl Mech Eng* 200:614–625
- Gao W, Yu SW, Huang GY (2006) Finite element characterization of the size-dependent mechanical behaviour in nanosystems. *Nanotechnology* 17(4):1118–1122
- Farsad M, Vernerey FJ, Park HS (2010) An extended finite element/level set method to study surface effects on the mechanical behavior and properties of nanomaterials. *Int J Numer Methods Eng* 84:1466–1489
- Gurtin ME, Murdoch A (1975) A continuum theory of elastic material surfaces. *Arch Ration Mech Anal* 57:291–323
- Javili A, Steinmann P (2009) A finite element framework for continua with boundary energies. part I: the two dimensional case. *Comput Methods Appl Mech Eng* 198:2198–2208
- Javili A, Steinmann P (2010) A finite element framework for continua with boundary energies. part II: the three dimensional case. *Comput Methods Appl Mech Eng* 199:755–765
- Park HS, Klein PA, Wagner GJ (2006) A surface cauchy-born model for nanoscale materials. *Int J Numer Methods Eng* 68:1072–1095
- Park HS, Klein PA (2007) Surface cauchy-born analysis of surface stress effects on metallic nanowires. *Phys Rev B* 75:085408
- Park HS, Klein PA (2008) A surface cauchy-born model for silicon nanostructures. *Comput Methods Appl Mech Eng* 197:3249–3260
- Javili A, McBride A, Steinmann P (2012) Thermomechanics of solids with lower-dimensional energetics: on the importance of surface, interface, and curve structures at the nanoscale a unifying review. *Appl Mech Rev* 65:010802
- Park HS, Klein PA (2008) Surface stress effects on the resonant properties of metal nanowires: the importance of finite deformation kinematics and the impact of the residual surface stress. *J Mech Phys Solids* 56:3144–3166
- Natarajan S, Chakraborty S, Thangavel M, Bordas S, Rabczuk T (2012) Size-dependent free flexural vibration behavior of functionally graded nanoplates. *Comput Mater Sci* 65:74–80
- Yun G, Park HS (2009) Surface stress effects on the bending properties of fcc metal nanowires. *Phys Rev B* 79:195421
- He J, Lilley CM (2008) Surface effect on the elastic behavior of static bending nanowires. *Nano Lett* 8(7):1798–1802
- Bendsoe MP, Kikuchi N (1988) Generating optimal topologies in structural design using a homogenization method. *Comput Methods Appl Mech Eng* 71:197–224
- Allaire G, Jouve F, Toader AM (2004) Structural optimization using sensitivity analysis and a level-set method. *J Comput Phys* 194:363–393
- Luo Z, Wang MY, Wang S, Wei P (2008) A level set-based parameterization method for structural shape and topology optimization. *Int J Numer Methods Eng* 76(1):1–26
- Melenk JM, Babuska I (1996) The partition of unity finite element method: basic theory and applications. *Comput Methods Appl Mech Eng* 139(1–4):289–314
- Osher SJ, Sethian JA (1988) Fronts propagating with curvature dependent speed: algorithms based on the Hamilton-Jacobi formulation. *J Comput Phys* 79:12–49
- Sethian JA, Wiegmann A (2000) Structural boundary design via level set and immersed interface methods. *J Comput Phys* 163:489–528
- Osher S, Santosa F (2001) Level-set methods for optimization problem involving geometry and constraints: I frequencies of a two-density inhomogeneous drum. *J Comput Phys* 171:272–288
- Wang MY, Wang XM, Guo DM (2003) A level set method for structural topology optimization. *Comput Methods Appl Mech Eng* 192:217–224
- Nanthakumar SS, Lahmer T, Rabczuk T (2014) Detection of multiple flaws in piezoelectric structures using XFEM and level sets. *Comput Methods Appl Mech Eng* 275:98–112
- Choi KK, Kim NH (2005) Structural sensitivity analysis and optimization. Springer, New York
- van Dijk NP, Maute K, Langelaar M, Keulen FV (2013) Level-set methods for structural topology optimization: a review. *Struct Multidiscip Optim* 48:437–472
- Malladi R, Sethian JA, Vemuri BC (1995) Shape modeling with front propagation: a level set approach. *IEEE Trans Pattern Anal Mach Intell* 17:158–175
- Stolarska M, Chopp DL, Moes N, Belytschko T (2001) Modeling crack growth by level sets in the extended finite element method. *Int J Numer Methods Eng* 51:943–960

39. Sukumar N, Chopp DL, Moes N, Belytschko T (2001) Modeling holes and inclusions by level sets in the extended finite-element method. *Comput Methods Appl Mech Eng* 190:6183–6200
40. Moes N, Cloirec M, Cartraud P, Remacle JF (2003) A computational approach to handle complex microstructure geometries. *Comput Methods Appl Mech Eng* 192:3163–3177
41. Craighead HG (2000) Nanoelectromechanical systems. *Science* 290:1532–1535
42. Ekinci KL, Roukes ML (2005) Nanoelectromechanical systems. *Rev Sci Instrum* 76:061101
43. Huang XMH, Zorman CA, Mehregany M, Roukes ML (2003) Nanodevice motion at microwave frequencies. *Nature* 42:496
44. Mi C, Jun S, Kouris DA, Kim SY (2008) Atomistic calculations of interface elastic properties in noncoherent metallic bilayers. *Phys Rev B* 77:075425
45. Ji C, Park HS (2006) Geometric effects on the inelastic deformation of metal nanowires. *Appl Phys Lett* 89:181916
46. Sigmund O (2001) A 99 line topology optimization code written in matlab. *Struct Multidiscip Optim* 21:120–127
47. Allaire G, Jouve F, Toader AM (2004) Structural optimization using sensitivity analysis and a level-set method. *J Comput Phys* 194:363–393